RSC Advances

PAPER

View Article Online
View Journal | View Issue

Cite this: *RSC Adv.*, 2020, **10**, 8905

A pressure-assisted annealing method for high quality $CsPbBr_3$ film deposited by sequential thermal evaporation†

Jingchen Hua,[a] Xi Deng,[a] Cheng Niu,[a] Fuzhi Huang,[a] Yong Peng,[a] Wangnan Li,*[b] Zhiliang Ku*[ab] and Yi-bing Cheng[ac]

Received 15th January 2020
Accepted 19th February 2020

DOI: 10.1039/d0ra00446d

rsc.li/rsc-advances

All-inorganic $CsPbBr_3$ perovskite solar cells have triggered incredible interest owing to their superior stability, especially under high temperature conditions. Different from the organic–inorganic hybrid perovskites, inorganic $CsPbBr_3$ perovskite always need a high annealing temperature for the formation of a cubic phase. Generally, the higher temperature (over 300 °C) and longer annealing time will promote the growth of $CsPbBr_3$, resulting in larger grain sizes and lower trap density in the crystals. However, $CsPbBr_3$ perovskite can also be damaged by excessive annealing temperature (~350 °C) and time, since $PbBr_2$ only has a melting temperature close to 357 °C. To address this issue, herein, we developed a novel pressure-assisted annealing method to prevent the sublimation of $PbBr_2$ at high temperature. The $CsPbBr_3$ films were firstly deposited by sequential thermal evaporation, and then annealed at 335 °C in an alloy pressure vessel. By controlling the pressure of the vessel, we obtained $CsPbBr_3$ films with various morphologies. At normal atmospheric pressure, the as-prepared $CsPbBr_3$ film exhibited small grain sizes and was full of pinholes. With the increase of annealing pressure, the grain sizes of the film showed a significant increasing trend, and the pinholes gradually vanished. When the pressure value came to 10 MPa, compact and uniform $CsPbBr_3$ films with large grain sizes were obtained. Based on these films, $CsPbBr_3$ perovskite solar cells with FTO/compact-TiO_2/$CsPbBr_3$/carbon architecture achieved a champion power conversion efficiency of 7.22%.

Introduction

In recent years, the metal halide perovskites have attracted enormous attention due to their extraordinary optical and electronic properties.[1–3] These unique features render such perovskite materials promising candidates for various optoelectronic devices, especially for solar cells. Till now, the record power conversion efficiency (PCE) of organic–inorganic hybrid perovskite solar cells (PSCs) has reached 25.2%,[4] which is on par with monocrystalline silicon solar cell. However, the organic components in hybrid perovskites might be a major constraint to the commercialization of PSCs, owing to their intrinsic instability under conditions such as heat,[5,6] electric field[7,8] and light illumination.[9–11] It should be noted that all of these conditions will not change even if the solar devices are well encapsulated. To break this impasse, more and more researchers shift their attentions toward all-inorganic perovskite,[12,13] which with inorganic Cs ion in place of the organic methylammonium or formamidinium cations. $CsPbI_3$ perovskite with a bandgap of 1.73 eV is suitable for capturing enough sunlight, and could reach 28.9% theoretical PCE according to the Shockley–Queisser limit.[14] To date, a record PCE of 19.03% has been reported in the FTO/compact-TiO_2/$CsPbI_3$/spiro-OMeTAD/Ag architecture.[15] However, the desired black cubic phase of $CsPbI_3$ perovskite is only stable at high temperature over 300 °C, and spontaneously transforms to the yellow orthorhombic phase under ambient environment.[16] Several strategies have been explored to stable the black cubic phase of $CsPbI_3$ perovskite at room temperature, including of decreasing the crystal size,[17] ion doping[18] and surface modification.[19] But still, the phase stability of $CsPbI_3$ perovskite is far away to meet the requirement for practical applications.

Full-brominated $CsPbBr_3$ perovskite presents an yellow orthorhombic phase at room temperature and transforms to a tetragonal phase at 88 °C and to the orange cubic phase at 130 °C.[20] Thanks to the wide band gap up to 2.3 eV, $CsPbBr_3$ perovskite can maintain most of its light absorption capability

---

[a] *State Key Laboratory of Advanced Technologies for Materials Synthesis and Processing, International School of Materials Science and Engineering, Wuhan University of Technology, 122 Luoshi Road, Wuhan, Hubei, P. R. China. E-mail: zhiliang.ku@whut.edu.cn*

[b] *Hubei Key Laboratory of Low Dimensional Optoelectronic Material and Devices, Hubei University of Arts and Science, 296 Longzhong Road, Xiangyang, Hubei Province, P. R. China*

[c] *Department of Materials Science and Engineering, Monash University, Wellington Road, Clayton, VIC3800, Australia*

† Electronic supplementary information (ESI) available. See DOI: 10.1039/d0ra00446d

during phase transition from cubic to orthorhombic. Thus, $CsPbBr_3$-PSCs have presented excellent moisture- and thermal-tolerance even in 95% RH and 100 °C respectively.[21] Despite $CsPbBr_3$ perovskite has a wide band gap, the high electron mobility and long electron life time[22] still make it become an idea light absorber. A high PCE of 10.9% (ref. 23) has been achieved in solar device with an architecture of FTO/compact-TiO_2/$CsPbBr_3$/spiro-OMeTAD/Ag. Moreover, the high open-circuit voltage (1.62 V)[24] together with the high transmittance in the visible region make such $CsPbBr_3$-PSCs to have significant potential for using in semitransparent building-integrated photovoltaics (BIPV) and tandem solar cells.[25] Unfortunately, for most of the high-performance $CsPbBr_3$-PSCs, solution-based techniques are still the first choice for the preparation of high quality $CsPbBr_3$ films.[26] Because of the poor solubility of CsBr in common solvents, CsBr always need several times coating on PbBr layer to obtain a desired $CsPbBr_3$ film thickness.[27] Obviously, the repetition of such solution-processing would be an obstacle for the reproducibility of large-area, uniform $CsPbBr_3$ film. In this regard, vacuum deposition is a more advantageous method for depositing films with large-size and good uniformity. But at present, there are few studies on the fabrication of $CsPbBr_3$-PSCs by using vacuum thermal evaporation.[28–32] In our previous work,[33,34] we demonstrated that introducing moderate moisture into the annealing process can help the crystallization of $CsPbBr_3$ perovskite. Actually, for $CsPbBr_3$ film deposited by sequential single-source vacuum deposition, the CsBr can hardly diffuse in the film to react properly with $PbBr_2$ in completely "dry condition". Hence, developing new annealing method to promote the growth of $CsPbBr_3$ in inert atmosphere is of great significance, especially for the vacuum process.

In this work, we annealed the vacuum-deposited $CsPbBr_3$ film in an alloy pressure vessel at 335 °C. To investigate how pressure affects the crystallization of $CsPbBr_3$ perovskite, we adjusted the vessel pressure value from 2 MPa to 10 MPa by controlling the compressed argon gas. As a contrast, $CsPbBr_3$ also annealed at 335 °C under standard atmospheric pressure (0.1 MPa). Not surprisingly, the film annealed in the pressure of 0.1 MPa (denoted as AP-0.1) was covered with small grains and full of pinholes. With the increasing of annealing pressure, the $CsPbBr_3$ film gradually enlarged their grain sizes and the pinholes vanished. As a result, the AP-10 sample showed a dense and uniform morphology with large grains, owing to the complete reaction between CsBr and $PbBr_2$ at high temperature and pressure. By using the as-prepared AP-10 $CsPbBr_3$ films, we fabricated PSCs with planar architecture of FTO/compact-TiO_2/$CsPbBr_3$/carbon. The devices achieved a champion PCE of 7.22%, which is much higher than that of the AP-0.1 $CsPbBr_3$ films. This pressure-assisted annealing method could provide a new way of preparing high-quality, large-area $CsPbBr_3$ films by vacuum deposition.

Experimental

Device fabrication

The FTO glass (Universal Laser Systems, VLS2.30) etched by femtosecond laser was firstly cleaned by detergent solution, deionized water and anhydrous ethanol, respectively. Then, the cleaned FTO glass was soaked into the $TiCl_4$ (99.5%, Aladdin) aqueous solution (0.05 M) for 30 min at 70 °C and then washed with DI water. Afterwards, the substrate was annealed at 450 °C for the formation of compact TiO_2 on FTO substrate. For the deposition of perovskite, CsBr (99.999%, Sigma-Aldrich) and $PbBr_2$ (99.99%, Xi'an p-OLED Corp.) were successively deposited with a rate of 5 Å on the compact TiO_2 layer by thermal evaporation, and this procedure was repeat for another time for desired thickness (~600 nm). Afterward, the as-deposited composite films were annealed in an alloy vessel to form $CsPbBr_3$ perovskite under argon atmosphere. By controlling the annealing pressure from room pressure to 10 MPa, we obtained different $CsPbBr_3$ samples. The annealing temperature was set at 335 °C and the heating rate was 15 °C min^{-1}. After annealed for 30 min, the $CsPbBr_3$ films were naturally cooled down to room temperature. Then, carbon electrode was deposited by screen-printing the carbon paste (Shitiao Printing Equipment Technology Co. Ltd) on the $CsPbBr_3$ layer. Finally, the device was dried on a hotplate at 100 °C for 10 min to remove the solvent in carbon paste.

Characterization

The X-ray diffraction (XRD) patterns of the samples are recorded using an X-ray diffractometer (XRD, D8 Advance). The absorbance spectra of inorganic perovskite films are recorded by using UV-vis (Lambda 750S, PerkinElmer). The steady-state photoluminescence (PL) spectra and the time-resolved photoluminescence (TRPL) are obtained by using PL microscopic spectrometer (Flex One, Zolix, China) and Delta Flex Fluorescence Lifetime System (Horiba Scientific Com., Japan), respectively. The morphology and composition are observed by a field-emission scanning electron microscopy (FE-SEM, Zeiss Ultra Plus). The current density–voltage (J–V) curves are measured using a solar simulator (Oriel 94023A, 300 W) with a source meter (Keithley 2400) under 100 mW cm^{-2} illumination (AM 1.5G) with a scan rate of 10 mV s^{-1}. The active area of the PSCs is 0.16 cm^2. The long-term thermal stability measurements were carried out in a environmental chamber (Weiss SC3 600 MHG).

Results and discussion

As shown in Fig. 1, $CsPbBr_3$ films were prepared *via* a multi-step sequential dual-source vacuum deposition (MS-DSVD) method.[33] In brief, CsBr and $PbBr_2$ were firstly deposited layer by layer with an overall thickness of ~600 nm, and then the composite films were transferred straightly from the vacuum

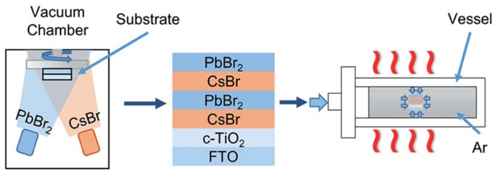

Fig. 1 Schematic illustration for the deposition of $CsPbBr_3$ films by MS-DSVD method and the pressure-assisted annealing process.

chamber into an alloy vessel for annealing (335 °C). The pressure of the vessel can be increased by argon gas cylinder, and the pressure value can be digitally controlled by a gas valve. To study the influence of pressure on the annealing affect, we annealed the samples under 2 MPa, 4 MPa, 6 MPa, 8 MPa and 10 MPa, respectively. Meanwhile, some control samples were annealed in room pressure (0.1 MPa, denoted as AP-0.1). Interesting, as the increasing of annealing pressure from 0.1 MPa to 10 MPa, the transmittance of $CsPbBr_3$ films was enhanced gradually (Fig. S1†).

Scanning electron microscopy (SEM) measurement was used to investigate the microstructure of the as-prepared $CsPbBr_3$ films. Top-view and cross-section SEM images of the AP-0.1–10 samples are shown in Fig. 2. Clearly, plenty of pinholes can be observed from surface of the entire AP-0.1 film (Fig. 2a). Moreover, most of the crystals exhibited a grain size around 300–500 nm. And grain boundaries that are parallel to the surface can be seen in the cross-section image, indicating the poor quality of $CsPbBr_3$ crystals. Meanwhile, the atomic force microscopy (AFM) measurement was used to quantitatively characterize the surface roughness of these films (Fig. S2†). As expected, a high root-mean-square (RMS) of surface roughness up to 38.4 nm was measured in the AP-0.1 film. We ascribe the poor crystallinity to the crystal growth characteristics of $CsPbBr_3$ perovskite. The volume will significantly expand upon phase conversion from $PbBr_2$ to $CsPbBr_3$ perovskite, leaving residual stress or pinholes among grains when the $PbBr_2$ films are over-compact.[24] As shown in the cross-section image of Fig. 2a, the extrusion of the grains against each other results in partial convex grains, leaving a large number of closed pores in the $CsPbBr_3$ film.[23] However, when we increased the annealing pressure to 2 MPa, the number of pinholes declined dramatically (Fig. 2b). The elimination of pinholes should be attribute to the high annealing pressure. Since the $PbBr_2$ only has a melting temperature close to 357 °C, annealing at 335 °C in high pressure could help the $PbBr_2$ maintain its melting state. As a result, the diffusion rate of $PbBr_2$ can be accelerated, rendering the formation of uniform $CsPbBr_3$ film without pinholes. At the same time, most of the $CsPbBr_3$ grains grew up to 400–600 nm, and the film surface became more flat (Ra = 30.8 nm). By further increasing the annealing pressure, we found the grain sizes of $CsPbBr_3$ continued to grow. When the pressure reached 6 MPa, a large number of $CsPbBr_3$ crystals with grain sizes of ~1 μm can be observed, and the pinholes nearly disappeared (Fig. 2d). As for the AP-8 and AP-10 samples (Fig. 2e and f), both of which showed a pinhole-free morphology with average grain sized over 1.5 μm. And the cross-sectional images revealed that the films possessed vertical and monolayer-aligned grains. Thus, the photo generated carriers could transfer in the out-of-plane directions across the perovskite layer towards the electrodes without passing through grain boundaries, which is conducive to obtaining a maximize charge transportation kinetics.[29,35] AFM images displayed in Fig. S2e and f† certified that both the AP-8 and AP-10 films exhibited a surface roughness around 21 nm, which was much lower than the evaporated $CsPbBr_3$ films in other reports.[28,29]

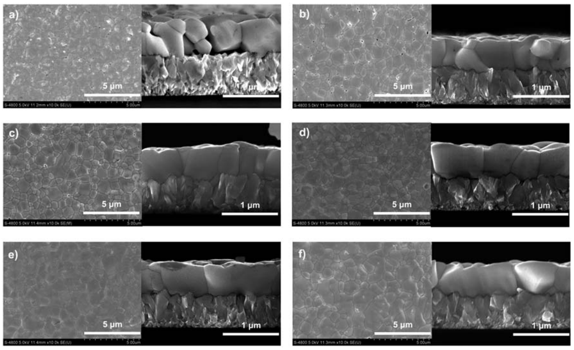

Fig. 2 Top-view and cross-sectional SEM images of $CsPbBr_3$ films with annealing pressure of (a) 0.1 MPa, (b) 2 MPa, (c) 4 MPa, (d) 6 MPa, (e) 8 MPa and (f) 10 MPa.

To identify the crystal structure of the $CsPbBr_3$ films, X-ray diffraction (XRD) characterizations were conducted on the as-prepared samples. As shown in Fig. 3, all samples exhibited similar diffraction patterns. The peaks at 2θ of 15.3°, 21.2°, 30.8°, and 34.4° should be ascribed to the diffraction of (100), (110), (200) and (210) crystal planes, indicating the formation of cubic $CsPbBr_3$ phase. So generally, the pressures had no significant influence on the crystal structure of $CsPbBr_3$. But it should be noticed that, as the increasing of annealing pressure, the crystallinity of $CsPbBr_3$ was improved markedly. Table S1† compared the characteristic peak intensity of FTO substrate ((110) plane, $2\theta = 26.6°$) and the (200) plane of $CsPbBr_3$. If we take the peak intensity of FTO-(110) as a constant, the ratio of $CsPbBr_3$-(200)/FTO-(110) could qualitatively reflect the crystallinity of $CsPbBr_3$. As expected, the AP-10 $CsPbBr_3$ possessed the highest ratio of 2.16, which is double that of the AP-0.1 $CsPbBr_3$. Basically, these results are consistent with the SEM images.

The optical and photoelectric properties of the $CsPbBr_3$ films were studied by UV-vis absorbance spectra and photoluminescence (PL) spectra. Fig. 4a showed the absorption spectra of the $CsPbBr_3$ films. All the films possessed an absorption edge at ~540 nm, which is characteristic of $CsPbBr_3$ perovskite.[3] As the annealing pressure increased, the absorbance of the films was enhanced, which can be explained by the better crystallinity and uniform grain size.[23] From the Tauc plot (Fig. S3†) of $(\alpha h\nu)^2$ *versus* photon energy ($h\nu$), the bandgaps of $CsPbBr_3$ films were calculated to be 2.35–2.36 eV by the Kubelka–Munk equation.[13] As for the transmittance spectra at long wavelength region from 550 nm to 800 nm, the AP-10 film

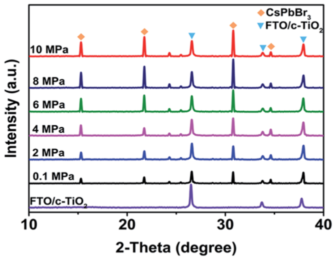

Fig. 3 XRD patterns of the $CsPbBr_3$ perovskite films prepared with different annealing pressures.

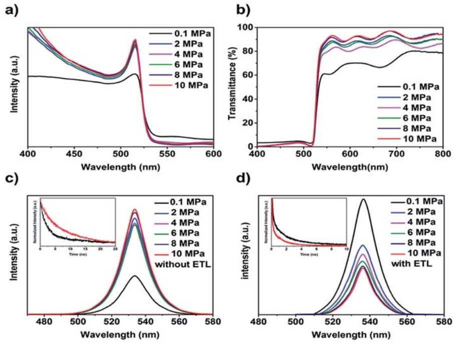

Fig. 4 (a) UV-vis absorption spectra and (b) transmittance spectra of the $CsPbBr_3$ films with different annealing pressures; steady-state photoluminescence of the $CsPbBr_3$ films deposited on substrate (c) with and (d) without electron transport layer. The inset of (c and d) are the corresponding time-resolved photoluminescence spectra of AP-0.1 and AP-10 sample.

showed the highest transparency (Fig. 4b), indicating a dense and smooth morphology with lowest light scattering.

Steady-state PL and time-resolved PL spectroscopy were used to investigate the non-radiative recombination process in the $CsPbBr_3$ films. As presented in Fig. 4c, without the electron transport layer (ETL), the intensity of the peaks at ~540 nm increased significantly as the increasing of annealing pressure. The enhanced PL intensity can be attributed to the improved crystallinity of the film with large grains size. The corresponding TRPL decay curves of the AP-0.1 and AP-10 films were presented in Fig. 4c (insert). By using bi-exponential decay function,[28] the curves were fitted to determine the decay times of the fast (τ_1) and slow (τ_2) components and the results were listed in Table S2.† The AP-0.1 and AP-10 films exhibited average carrier lifetimes (τ_{avg}) of 3.35 and 8.99 ns, respectively. In general, the longer carrier lifetime always coincided with a slower carrier recombination rate, inducing by low trap-state density in the films. For further understanding the intrinsic recombination behaviour of the solar devices, we studied the relationship between V_{oc} and various incident light intensities (I_{light}) of the devices. Generally, the function of V_{oc} and I_{light} can be described and fitted *via* the following formula:[36] $V_{oc} \propto nkT\ln(I_{light})/q$, where n represent factors relate to bimolecular and trap-assisted recombination, k represents Boltzmann constant, T is absolute temperature in kelvin, q is an elementary charge. As shown in Fig. S4,† the n value of AP-10 device (1.73) is much smaller than that of the AP-0.1 device, suggesting lower trap-assisted recombination in the device.

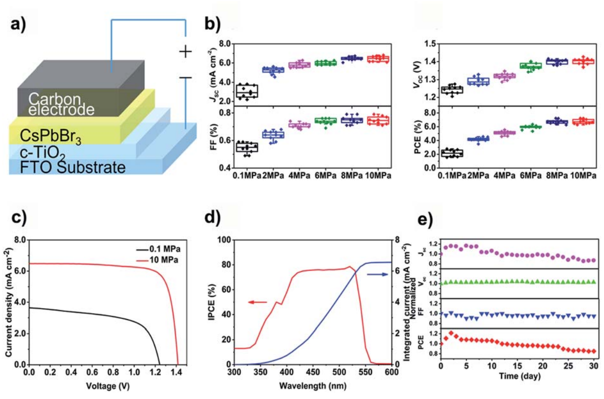

Fig. 5 (a) Device structure of $CsPbBr_3$ PSCs; (b) the distribution diagram of photovoltaic parameters of $CsPbBr_3$ PSCs with different annealing pressures; (c) *J–V* curves and (d) IPCE of the champion device; (e) long-term stability of the device under condition of 100 °C with 80% humidity.

In addition, we also performed the steady-state PL measurement on the $CsPbBr_3$ films with FTO/compact-TiO_2 substrates. As shown in Fig. 4d, the AP-10 sample exhibited a dramatically high degree of PL quenching in comparison with the AP-0.1 sample. Generally, this PL quenching is attributed to the efficient electron extraction across the perovskite/TiO_2 interface. The charge lifetime obtained from TRPL decay curves (insert of Fig. 4d) further confirmed that the charge carrier extraction at the $CsPbBr_3$/TiO_2 interface could be enhanced by the annealing pressure.

To further verify the enhancement of crystal quality of $CsPbBr_3$ films by high pressure annealing. All-inorganic PSCs with FTO/compact-TiO_2/$CsPbBr_3$/carbon architecture (Fig. 5a) were fabricated based on the as-prepared $CsPbBr_3$ films. 60 devices were divided into 6 batches and each batch consists of 10 cells with the same annealing pressure. The current–voltage (*J–V*) performances of the devices were measured under one sun illumination (AM 1.5G). The distribution diagram of photovoltaic parameters (short-circuit current density (J_{sc}), open-circuit voltage (V_{oc}), fill factor (FF) and power conversion efficiency (PCE)) were summarized in Fig. 5b. Clearly, with the increase of annealing pressure, all the *J–V* parameters improved significantly. The best device based on PA-0.1 films displayed a J_{sc} of 3.69 mA cm^{-2}, a V_{oc} of 1.26 V, a FF of 0.60, rendering a poor PCE of 2.79%. However, with the AP-10 films, the champion device achieved a J_{sc} of 6.49 mA cm^{-2}, a V_{oc} of 1.42 V, a FF of 0.79, with an overall PCE of 7.22% (Fig. 5c). The enhancement of photocurrent was checked by the photon-to-electron conversion efficiency (IPCE) measurement. As shown in Fig. 5d, the champion device exhibited a high IPCE value of ~80% over the whole wavelength range of 450–525 nm. The integrated J_{sc} reached 6.43 mA cm^{-2}, which is coincidence with the *J–V* result. Moreover, the long-term stability of the champion device was tested under 100 °C & RH = 80% condition without encapsulation. As shown in Fig. 5e, the device maintained 80% of its initial PCE over 30 days, showing excellent moisture and heat tolerance.

Conclusions

In summary, we developed a novel pressure-assisted annealing method for the preparation of high quality $CsPbBr_3$ films. At standard atmospheric pressure (0.1 MPa), the $CsPbBr_3$ film annealed at 335 °C exhibited poor crystallinity and high surface roughness with many pinholes. However, when we increased the pressure up to 10 MPa, the resulting $CsPbBr_3$ film displayed a dense and smooth morphology with large average grain sizes over 1.5 μm. Further PL measurements revealed that the trap-state density in $CsPbBr_3$ film can be dramatically decreased by the pressure. To identify the positive effect of annealing pressure on the optoelectronic performance of the $CsPbBr_3$ film, we fabricated PSCs based on $CsPbBr_3$ films annealed at different pressure. As a result, the device with the $CsPbBr_3$ film annealed at 10 MPa showed a champion PCE of 7.22%, which was much higher than that with the film annealed at 0.1 MPa. We believe that this pressure-assisted annealing method could open a new path for achieving high-quality evaporated $CsPbBr_3$ films.

Conflicts of interest

There are no conflicts to declare.

Acknowledgements

The authors acknowledge the financial support by National Natural Science Foundation of China (NSFC 51702243, 51972251, 91963209), the National Key Research and Development Program of China (No. 2018YFB1500104) and the Fundamental Research Funds for the Central Universities (WUT: 2016IVA093, 2017III022, 2018IVB031).

Notes and references

1 G. Xing, N. Mathews, S. Sun, S. S. Lim, Y. M. Lam, M. Gratzel, S. Mhaisalkar and T. C. Sum, *Science*, 2013, **342**, 344–347.

2 S. D. Stranks, G. E. Eperon, G. Grancini, C. Menelaou, M. J. Alcocer, T. Leijtens, L. M. Herz, A. Petrozza and H. J. Snaith, *Science*, 2013, **342**, 341–344.

3 M. I. Saidaminov, A. L. Abdelhady, B. Murali, E. Alarousu, V. M. Burlakov, W. Peng, I. Dursun, L. Wang, Y. He, G. Maculan, A. Goriely, T. Wu, O. F. Mohammed and O. M. Bakr, *Nat. Commun.*, 2015, **6**, 1–6.

4 *N. R. E. L. N. Best Research Cell_Efficiencies*, 2019, https://www.nrel.gov/pv/cell-efficiency.html.

5 E. J. Juarez-Perez, Z. Hawash, S. R. Raga, L. K. Ono and Y. Qi, *Energy Environ. Sci.*, 2016, **9**, 3406–3410.

6 A. Dualeh, P. Gao, S. I. Seok, M. K. Nazeeruddin and M. Grätzel, *Chem. Mater.*, 2014, **26**, 6160–6164.

7 W. Tress, M. Yavari, K. Domanski, P. Yadav, B. Niesen, J. P. Correa Baena, A. Hagfeldt and M. Graetzel, *Energy Environ. Sci.*, 2018, **11**, 151–165.

8 O. R. Yamilova, A. V. Danilov, M. Mangrulkar, Y. S. Fedotov, S. Y. Luchkin, S. D. Babenko, S. I. Bredikhin, S. M. Aldoshin, K. J. Stevenson and P. A. Troshin, *J. Phys. Chem. Lett.*, 2019, 221–228, DOI: 10.1021/acs.jpclett.9b03161.

9 R. K. Misra, S. Aharon, B. Li, D. Mogilyansky, I. Visoly-Fisher, L. Etgar and E. A. Katz, *J. Phys. Chem. Lett.*, 2015, **6**, 326–330.

10 S. Chen, X. Du, D. Lin, F. Xie, W. Xie, L. Gong, W. Zhang, P. Liu and J. Chen, *J. Electron Spectrosc. Relat. Phenom.*, 2018, **229**, 108–113.

11 Q.-M. Hong, R.-P. Xu, T.-Y. Jin, J.-X. Tang and Y.-Q. Li, *Org. Electron.*, 2019, **67**, 19–25.

12 G. E. Eperon, G. M. Paternò, R. J. Sutton, A. Zampetti, A. A. Haghighirad, F. Cacialli and H. J. Snaith, *J. Mater. Chem. A*, 2015, **3**, 19688–19695.

13 M. Kulbak, D. Cahen and G. Hodes, *J. Phys. Chem. Lett.*, 2015, **6**, 2452–2456.

14 J. Duan, H. Xu, W. E. I. Sha, Y. Zhao, Y. Wang, X. Yang and Q. Tang, *J. Mater. Chem. A*, 2019, **7**, 21036–21068.

15 Y. Wang, X. Liu, T. Zhang, X. Wang, M. Kan, J. Shi and Y. Zhao, *Angew. Chem., Int. Ed.*, 2019, **58**, 16691–16696.

16 S. Dastidar, C. J. Hawley, A. D. Dillon, A. D. Gutierrez-Perez, J. E. Spanier and A. T. Fafarman, *J. Phys. Chem. Lett.*, 2017, **8**, 1278–1282.

17 A. Swarnkar, A. R. Marshall, E. M. Sanehira, B. D. Chernomordik, D. T. Moore, J. A. Christians, T. Chakrabarti and J. M. Luther, *Science*, 2016, **354**, 92–95.

18 A. K. Jena, A. Kulkarni, Y. Sanehira, M. Ikegami and T. Miyasaka, *Chem. Mater.*, 2018, **30**, 6668–6674.

19 Y. Fu, M. T. Rea, J. Chen, D. J. Morrow, M. P. Hautzinger, Y. Zhao, D. Pan, L. H. Manger, J. C. Wright, R. H. Goldsmith and S. Jin, *Chem. Mater.*, 2017, **29**, 8385–8394.

20 H. L. Wells, *Z. Anorg. Chem.*, 1893, **3**, 195–210.

21 J. Liang, C. X. Wang, Y. R. Wang, Z. R. Xu, Z. P. Lu, Y. Ma, H. F. Zhu, Y. Hu, C. C. Xiao, X. Yi, G. Y. Zhu, H. L. Lv, L. B. Ma, T. Chen, Z. X. Tie, Z. Jin and J. Liu, *J. Am. Chem. Soc.*, 2016, **138**, 15829–15832.

22 C. C. Stoumpos, C. D. Malliakas, J. A. Peters, Z. Liu, M. Sebastian, J. Im, T. C. Chasapis, A. C. Wibowo, D. Y. Chung, A. J. Freeman, B. W. Wessels and M. G. Kanatzidis, *Cryst. Growth Des.*, 2013, **13**, 2722–2727.

23 G. Tong, T. Chen, H. Li, L. Qiu, Z. Liu, Y. Dang, W. Song, L. K. Ono, Y. Jiang and Y. Qi, *Nano Energy*, 2019, **65**, 104015.

24 Y. Zhao, J. Duan, Y. Wang, X. Yang and Q. Tang, *Nano Energy*, 2019, 104286, DOI: 10.1016/j.nanoen.2019.104286.

25 W. Chen, J. Zhang, G. Xu, R. Xue, Y. Li, Y. Zhou, J. Hou and Y. Li, *Adv. Mater.*, 2018, **30**, 1800855.

26 J. Zhang, G. Hodes, Z. Jin and S. Liu, *Angew. Chem., Int. Ed.*, 2019, **58**, 15596–15618.

27 J. Duan, Y. Zhao, X. Yang, Y. Wang, B. He and Q. Tang, *Adv. Energy Mater.*, 2018, **8**, 1802346.

28 J. Lei, F. Gao, H. Wang, J. Li, J. Jiang, X. Wu, R. Gao, Z. Yang and S. Liu, *Sol. Energy Mater. Sol. Cells*, 2018, **187**, 1–8.

29 X. Liu, X. Tan, Z. Liu, B. Sun, J. Li, S. Xi, T. Shi and G. Liao, *J. Power Sources*, 2019, **443**, 227269.

30 Y. El Ajjouri, F. Palazon, M. Sessolo and H. J. Bolink, *Chem. Mater.*, 2018, **30**, 7423–7427.

31 W. Chen, J. Zhang, G. Xu, R. Xue, Y. Li, Y. Zhou, J. Hou and Y. Li, *Adv. Mater.*, 2018, **30**, e1800855.

32 H. Li, G. Tong, T. Chen, H. Zhu, G. Li, Y. Chang, L. Wang and Y. Jiang, *J. Mater. Chem. A*, 2018, **6**, 14255–14261.

33 Y. Zhang, L. Luo, J. Hua, C. Wang, F. Huang, J. Zhong, Y. Peng, Z. Ku and Y.-b. Cheng, *Mater. Sci. Semicond. Process.*, 2019, **98**, 39–43.

34 T. Xiang, Y. Zhang, H. Wu, J. Li, L. Yang, K. Wang, J. Xia, Z. Deng, J. Xiao, W. Li, Z. Ku, F. Huang, J. Zhong, Y. Peng and Y.-B. Cheng, *Sol. Energy Mater. Sol. Cells*, 2019, 110317, DOI: 10.1016/j.solmat.2019.110317.

35 J. Xiao, Y. Yang, X. Xu, J. Shi, L. Zhu, S. Lv, H. Wu, Y. Luo, D. Li and Q. Meng, *J. Mater. Chem. A*, 2015, **3**, 5289–5293.

36 M. J. Speirs, D. N. Dirin, M. Abdu-Aguye, D. M. Balazs, M. V. Kovalenko and M. A. Loi, *Energy Environ. Sci.*, 2016, **9**, 2916–2924.